

Variational preparation of entangled states in a system of transmon qubits

Alexander Yeremeyev,^{1, 2, *} Aleksei Tolstobrov,^{1, 2} Gleb Fedorov,^{2, 3} Shtefan Sanduleanu,^{2, 3} Peter Shlykov,^{1, 2} Sergey Samarin,^{1, 2} Shamil Kadrymetov,² Artyom Muraviev,^{1, 2} Aleksey Bolgar,² Daria Kalacheva,² Viktor Lubsanov,² Aleksei Dmitriev,^{2, 3} Evgenia Alekseeva,² and Oleg V. Astafiev^{1, 2}

¹*Center for Engineering Physics, Skolkovo Institute of Science and Technology, 121205 Moscow, Russia*

²*Laboratory of Artificial Quantum Systems, Moscow Center for Advanced Studies, 123592 Moscow, Russia*

³*Kotel'nikov Institute of Radio Engineering and Electronics,*

Russian Academy of Sciences, 125009 Moscow, Russia

(Dated: April 22, 2025)

The conventional method for generating entangled states in qubit systems relies on applying precise two-qubit entangling gates alongside single-qubit rotations. However, achieving high-fidelity entanglement demands high accuracy in two-qubit operations, requiring complex calibration protocols. In this work, we use a minimally calibrated two-qubit iSwap-like gate, tuned via straightforward parameter optimization (flux pulse amplitude and duration), to prepare Bell states and GHZ states experimentally in systems of two and three transmon qubits. By integrating this gate into a variational quantum algorithm (VQA), we bypass the need for intricate calibration while maintaining high fidelity. Our proposed methodology employs variational quantum algorithms (VQAs) to create the target quantum state through imperfect multiqubit operations. Furthermore, we experimentally demonstrate a violation of the Clauser–Horne–Shimony–Holt (CHSH) inequality for Bell states, confirming their high fidelity of preparation.

Keywords: variational quantum algorithms, transmon qubits, Bell states, GHZ state, CHSH inequality violation.

I. INTRODUCTION

Recent research in quantum technologies has seen growing interest in applying machine learning to experiments with various quantum systems. Machine learning has demonstrated potential for qubit control through pulse optimization, enabling tasks such as multi-qubit state preparation [1] and single-qubit gate optimization [2].

For noisy intermediate-scale quantum systems [3], where the limited number of qubits and the absence of error correction prevent direct realization of quantum advantage, variational quantum algorithms (VQAs) have been successfully applied to tasks such as state preparation [4], classification [5–10], image recognition [9, 11], and simulating quantum systems [12]. Recently, variational quantum algorithms have been theoretically explored as a tool for generating multi-qubit entangled states [13]. However, the scheme discussed in that work does not seem to be practically feasible because it relies on the knowledge of the explicit form of the unitary transformation which generates the target state. As a result, that approach does not offer any advantages for real-world applications. In recent experimental works, VQAs have shown potential for preparing some specific mixed quantum states, such as thermal Gibbs states at various temperatures in a system of two transmon qubits [4].

In this work, we focus on the experimental variational preparation of two-qubit Bell states and the three-qubit Greenberger–Horne–Zeilinger (GHZ) state [14] using the

superconducting quantum computing platform. Typically, Bell states are generated using high-precision two-qubit entangling gates, such as $\sqrt{i}\text{Swap}$ [15, 16] or cPhase [17]. Obviously, the fidelity of the resulting states is highly sensitive to the accuracy of the gates, which in turn demands intricate calibration procedures [18]. To show that this challenge may be addressed, in this work we develop a fully automatic calibration routine based on a gradient-descent VQA that incorporates a quantum circuit comprising minimally calibrated fixed iSwap-like gates [19] and single-qubit X and Y rotations with tunable angles. Our approach introduces an alternative methodology for learning accurate quantum evolution using non-ideal multi-qubit gates, and, simultaneously, exhibits a clear example of a practical application for variational quantum algorithms in realistic experimental settings.

The minimally calibrated iSwap-like gate that we use emerges physically from the multi-level structure of transmons leading to an evolution combining the $|01\rangle \leftrightarrow |10\rangle$ iSwap interaction with residual phase shifts from unintended $|11\rangle \leftrightarrow |02\rangle$ cPhase coupling; additionally, single-qubit phases are accumulated. While in other applications such as digital quantum algorithms this kind of behavior may be regarded as disadvantageous, our approach instead leverages this native operation by compensating for its imperfections through variational optimization of surrounding single-qubit gates, reproducing high-fidelity state preparation.

We confirm the fidelity of the generated entangled states, by performing the quantum state tomography (QST) [20]. However, full QST is not necessary for entanglement verification, since Bell states exhibit strong correlations in measurements which may be revealed in

* Alexander.Yeremeyev@skoltech.ru

experiments requiring only single-qubit rotations and simultaneous measurement of qubit states. In 1964, Bell formulated an inequality for two entangled particles [21], providing a framework to experimentally test whether quantum mechanics is the best possible theory or whether there exist some underlying hidden local variables knowing which a better theory without uncertainty could be developed [22]. The Clauser–Horne–Shimony–Holt (CHSH) inequality, derived in 1969 [23], simplified the experimental verification of Bell’s theorem. We experimentally measured the violation of the CHSH inequality for the prepared Bell states, demonstrating their entanglement and nonclassical behavior.

II. EXPERIMENTAL DESIGN

The experiment was conducted on three transmon qubits [24] (I, II, and III, left to right) as shown in Figure 1a. The entire experimental sample incorporates 16 superconducting transmon artificial atoms (see Supplementary for full device characterization). The key properties of the studied transmons, including transition frequencies (ν_{01}), relaxation times (T_1), dephasing times (T_2^*), and their readout resonator frequencies (ν_r), are detailed in Table I. Experimental equipment, the measurement scheme is almost the same as described in the article [10].

As said above, we leverage the native iSwap-like gates realizing a population exchange between the $|01\rangle$ and $|10\rangle$ states in a pair of qubits. These gates are roughly calibrated by varying the amplitude and duration (with 1 ns resolution) of the flux pulse applied to one of the transmons and finding an optimum on a two-dimensional map of population transfer (data in Supplementary). To perform high-quality single-qubit rotations, we implemented the DRAG (Derivative Removal by Adiabatic Gate) calibration scheme [25, 26], which significantly mitigates leakage to higher transmon energy levels. Using single-qubit randomized benchmarking [27], we measured an average gate fidelity of 99.74% for single-qubit rotations of angles $\pi/2$ and π , confirming high-precision control of individual qubits in our system.

The transmons are read out using a frequency-multiplexed scheme [28] in single-shot mode [29], enabling the measurement of multi-qubit correlations. We use a Josephson parametric amplifier (JPA) [30] to enhance the signal-to-noise ratio for the single-shot readout. Given the resonator frequency separation of approximately 300–400 MHz between resonators neighboring qubits (see Table I), the readout accuracy achieved with a narrowband JPA was approximately 80–85%. To mitigate readout errors, we applied the inverse error matrix method [31], where the error matrix was measured directly after preparing the qubits in their basis states.

Table I. The measured parameters for the superconducting artificial atoms: ν_{01} - the frequency of the transition from the ground state $|0\rangle$ to the excited state $|1\rangle$, T_1 - the qubit relaxation time, characterizing energy decay, T_2^* - the qubit dephasing time, representing coherence loss, ν_r - the frequency of the resonator coupled to the transmon, and durations of two-qubit operation (iSwap-like gates) and single-qubit rotations.

Qubit	I	II	III
<i>sweet spot</i>	<i>bottom</i>	<i>top</i>	<i>bottom</i>
ν_{01} , GHz	4.228	4.747	4.497
T_1 , μ s	22	16	23
T_2^* , μ s	3.5	3.2	4.8
ν_r , GHz	6.717	6.436	6.827
<i>iSwap</i> , ns		37	26
X, Y , ns	40	40	40

III. PREPARATION OF BELL’S STATES AND GHZ STATE

Figure 1b,c illustrates the quantum circuit designed for preparing the two-qubit Bell states. The circuit comprises 12 parameterized single-qubit rotations, 6 around the X -axis and 6 around the Y -axis of the Bloch sphere, along with two non-ideal iSwap-like entangling operations. Following the state preparation block, the circuit includes a module for quantum state tomography and qubit measurement.

We begin the optimization procedure for generating the Bell states with preparation of the multi-qubit ground state $|\emptyset\rangle$. It is achieved through qubit relaxation, with a waiting time of approximately $5 T_1$ to ensure high-fidelity initialization; however, this does not reduce the presence of thermal population of the qubit [32]. Alternatively, active reset algorithms [33, 34] can be employed to significantly reduce the initialization time and accelerate the optimization process.

After the variational ansatz is applied, the loss function needs to be calculated. For the parameters vector $\boldsymbol{\theta} = \theta_{1-12}$ (at the first step of the algorithm it is determined by random values) of the single-qubit X, Y rotations, the probabilities of measuring the qubits in each of the four basis states $|00\rangle, |01\rangle, |10\rangle, |11\rangle$ are determined, see Figure 1b. For this purpose, we perform 2000 runs of the quantum circuit execution and average the results.

The loss function is then calculated as:

$$\mathcal{L} = \frac{1}{4N} \sum_{i=1}^N \sum_{j=1}^4 (p_{\text{targ}}^{(i,j)} - p_{\text{exp}}^{(i,j)})^2, \quad (1)$$

where j denotes the indices of the measured states, i represents the indices of the pre-measurement rotations: $X_{\varphi_1}, X_{\varphi_2}, Y_{\varphi_3}, Y_{\varphi_4} = \{[\mathbb{1}, \mathbb{1}], [\mathbb{1}, X_{\frac{\pi}{2}}], [X_{\frac{\pi}{2}}, \mathbb{1}]\} \otimes \{[\mathbb{1}, \mathbb{1}], [\mathbb{1}, Y_{\frac{\pi}{2}}], [Y_{\frac{\pi}{2}}, \mathbb{1}]\}$, N is number of all combinations of tomography rotations; finally, $p_{\text{targ}}^{(i,j)}$ are the theoretical probabilities for the target state and $p_{\text{exp}}^{(i,j)}$ are the

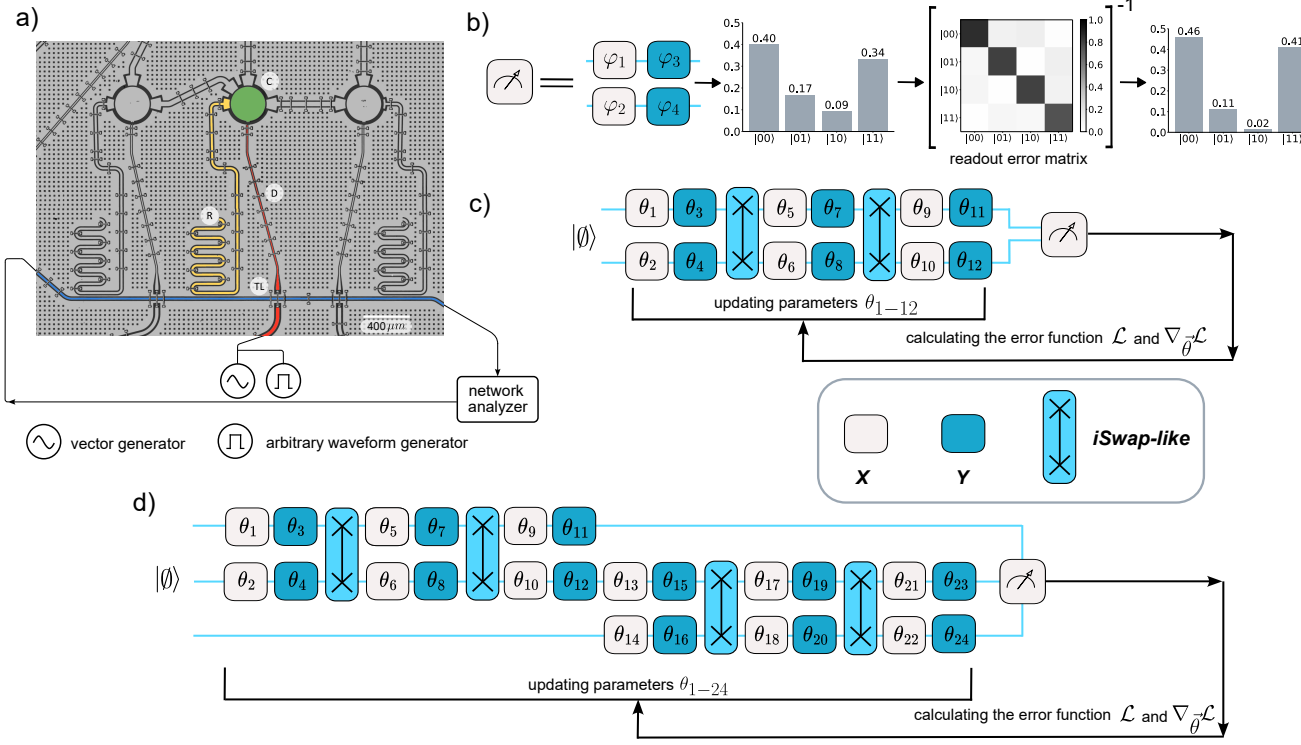


Figure 1. a) Micrograph of the three transmons used in this experiment (false-colored). Green (C) represents the transmon shunt capacitance, yellow (R) denotes the readout resonator, red (D) indicates the drive-bias control line, and blue (TL) corresponds to the transmission readout line. b) The state readout protocol involves three sequential steps: (1) tomography rotations to prepare various measurement bases, (2) statistical averaging through repeated measurements (about 2000 shots) to determine basis state populations, and (3) application of readout error correction using the inverse error matrix method. c) Quantum circuit for preparing Bell states with two qubits. d) Quantum circuit for preparing GHZ states with three qubits.

experimentally measured probabilities for the current set of parameters θ , including readout error correction. For example, for the Bell state $(|00\rangle + |11\rangle)/\sqrt{2}$ and rotations $\varphi_{1-4}^{(i=1)} = 0$ one has $p_{\text{targ}}^{(i=1, j=1:4)} = [0.5, 0, 0, 0.5]$. Usually, for a two-qubit system, quantum state tomography requires 15 distinct measurement bases with measurement of the correlator of qubit states to reconstruct the density matrix ρ . However, our protocol requires just $N = 9$ distinct measurement bases because we read out the populations of all basis states, which carries more information. Due to the normalization constraint, each basis yields 3 independent probability measurements, resulting in 27 total parameters for the loss function \mathcal{L} . This exceeds the 15 independent parameters needed to reconstruct the density matrix ρ , ensuring the generated state can be completely determined.

Finally, the protocol completes with updating the ansatz parameters θ . The parameters of the quantum circuit are optimized using Nesterov's accelerated gradient descent algorithm [35]. The gradients of the loss function with respect to the parameters are computed using the parameter-shift rule [36, 37], which enables efficient gradient estimation for variational quantum algorithms.

After the convergence is reached, we perform the usual QST for the Bell states based on the measurement results for all rotation angles combinations $\varphi_{1-4}^{(i)}$ via maximum likelihood estimation. The density matrix ρ is parameterized using the Cholesky decomposition. We calculated the measurement probabilities for current parametrization of density matrix using the cross-platform Python library PennyLane [38] for all tomography angles, and then the mean square of deviation from measured probabilities was calculated and minimized to reconstruct the density matrix.

Figure 2 presents the optimization data for one of the Bell states $|\beta_{00}\rangle = (|00\rangle + |11\rangle)/\sqrt{2}$: density matrices of the two-qubit states obtained from quantum state tomography (showing both real and imaginary parts), the dependence of the loss function \mathcal{L} on the algorithm iteration, the evolution of the parameters θ_{1-12} as a function of the algorithm iteration number.

The Supplementary information presents complete experimental results for all four Bell states. The fidelities $\mathcal{F} = \sqrt{\text{Tr}(\rho_{\text{exp}} \cdot \rho_{\text{targ}})}$ (ρ_{exp} is the reconstructed density matrix of the prepared state, ρ_{targ} is the density matrix of the target state) of the density matrices, along with

the standard deviations computed as the average over the last five steps of the algorithm, are summarized in Table II.

Bell State	Fidelity $\mathcal{F} \pm \sigma$	$\max(S_{1,2}) \pm \sigma$
$ \beta_{00}\rangle = \frac{1}{\sqrt{2}}(00\rangle + 11\rangle)$	0.949 ± 0.005	2.47 ± 0.08
$ \beta_{01}\rangle = \frac{1}{\sqrt{2}}(01\rangle + 10\rangle)$	0.987 ± 0.009	2.77 ± 0.10
$ \beta_{10}\rangle = \frac{1}{\sqrt{2}}(00\rangle - 11\rangle)$	0.930 ± 0.006	2.30 ± 0.11
$ \beta_{11}\rangle = \frac{1}{\sqrt{2}}(01\rangle - 10\rangle)$	0.956 ± 0.009	2.52 ± 0.11

Table II. Fidelities of generated Bell states with standard deviations and maximum values of CHSH inequality violation with standard deviations.

The next application of the variational quantum algorithm (VQA) is the preparation of the Greenberger–Horne–Zeilinger (GHZ) state: $(|000\rangle + |111\rangle)/\sqrt{2}$. This three-qubit entangled state represents a generalization of the Bell state to three qubits. The quantum circuit used for its preparation, shown in Figure 1d, extends the Bell state circuit incorporating 12 single-qubit rotations around the X -axis of the Bloch sphere, 12 single-qubit rotations around the Y -axis, and four native iSwap-like entangling operations.

The optimization process and density matrix tomography follow the same approach as described for the two-qubit case, generalized to three qubits. Since for a 3-qubit state the calculation of the loss function \mathcal{L} takes more time, the optimization was carried out as follows: the Bell state $\frac{1}{\sqrt{2}}(|00\rangle + |11\rangle)$, already obtained through optimization, was used as input, and parameters θ_{13-24} were optimized. After reaching convergence, we included all 24 parameters θ_{1-24} in the optimization. Figure 3 displays the real part of the reconstructed density matrix for the GHZ state obtained through variational circuit optimization and the values of the loss function throughout the algorithm iterations. The fidelity of the prepared state, calculated from the density matrix, is 0.869 ± 0.003 . Further details about the GHZ state preparation are provided in the Supplementary Materials.

IV. DEMONSTRATION OF CHSH INEQUALITY VIOLATIONS

We employ two combinations of correlators to measure the CHSH inequality:

$$S_1 = E(a, b) + E(a', b) + E(a, b') - E(a', b'), \quad (2)$$

and

$$S_2 = -E(a, b) - E(a', b) + E(a, b') - E(a', b'), \quad (3)$$

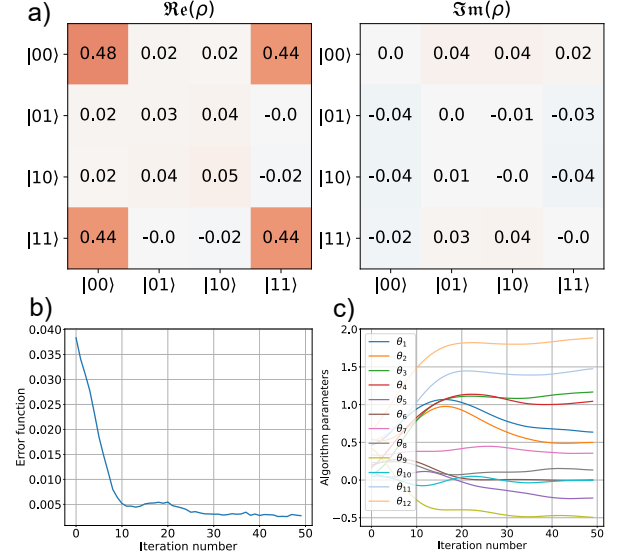


Figure 2. a) For the Bell state $\frac{1}{\sqrt{2}}(|00\rangle + |11\rangle)$, the figure presents the experimentally measured density matrix at the last iteration of the algorithm, showing both real and imaginary components. b) The evolution of the loss function \mathcal{L} as a function of algorithm iteration number, demonstrating the convergence behavior. c) The parameters optimization trajectory, showing the dependence of quantum circuit parameters on the algorithm iteration number.

where $E(a, b) = P_{a,b}(|00\rangle) - P_{a,b}(|10\rangle) - P_{a,b}(|01\rangle) + P_{a,b}(|11\rangle)$ is the correlator of measured states for two qubits at rotation angles a and b , and P denotes the probability of measuring one of the basis states for the two-qubit system.

The combination S_1 is used for the Bell states $|\beta_{00}\rangle = (|00\rangle + |11\rangle)/\sqrt{2}$ and $|\beta_{01}\rangle = (|01\rangle + |10\rangle)/\sqrt{2}$, while S_2 is applied to the states $|\beta_{10}\rangle = (|00\rangle - |11\rangle)/\sqrt{2}$ and $|\beta_{11}\rangle = (|01\rangle - |10\rangle)/\sqrt{2}$. For entangled states, the violation of the CHSH inequality requires $|\max(|S_1|)| > 2$ and $|\max(|S_2|)| > 2$, with the maximum theoretical value bounded by $2\sqrt{2}$ (Tsirelson's bound) [39].

Figure 4a presents the experimental measurements of the CHSH inequality violation. The rotation angles of the qubits around the X -axis of the Bloch sphere are defined as:

$$a' = a + \pi/2, \quad b' = b + \pi/2, \quad \theta = a - b.$$

The graph for one of the Bell states $|\beta_{00}\rangle = (|00\rangle + |11\rangle)/\sqrt{2}$ depicts the dependence of the correlators $E(a, b)$, $E(a', b)$, $E(a, b')$, and $E(a', b')$, as well as the expressions S_1 , on the angle θ . Each point is the result of averaging over 50 experiments; sticks show standard deviations. The Supplementary information presents CHSH inequality violation measurements for all four Bell states. The results demonstrate that the maximum values of $|S_{1,2}|$ exceed the classical limit of 2 for all Bell

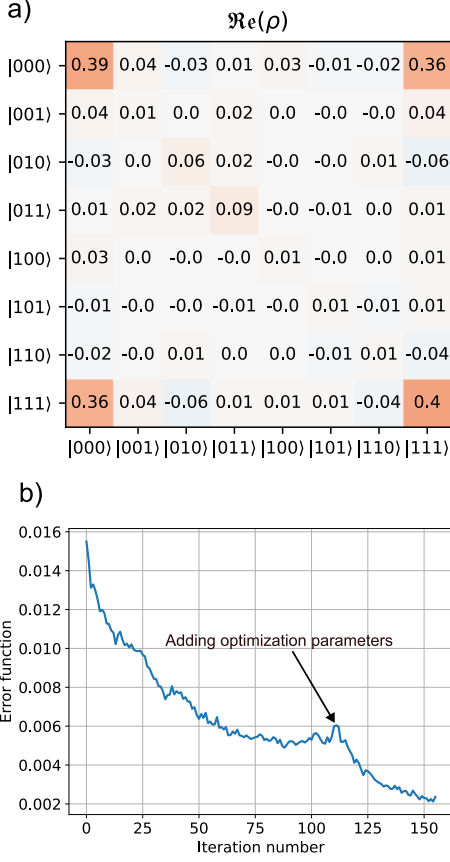


Figure 3. a) The real component of the reconstructed density matrix of the three-qubit GHZ state $\frac{1}{\sqrt{2}}(|000\rangle + |111\rangle)$ obtained after variational circuit optimization. b) The values of the error function throughout the algorithm iterations are shown. The training procedure was initialized with the state $\frac{1}{\sqrt{2}}(|00\rangle + |11\rangle)$, first optimizing parameters θ_{13-24} . The arrow indicates the transition point where optimization of all 24 parameters (θ_{1-24}) commenced.

states: $|\beta_{00}\rangle$, $|\beta_{01}\rangle$, $|\beta_{10}\rangle$, and $|\beta_{11}\rangle$. Specifically, the measured maxima are summarized in Table II.

At angles $\theta = \pi/2$ and π , notches in the correlators are observed. These arise due to the transition between $R_x(-\pi)$ and $R_x(\pi)$ rotations, which is sensitive to non-ideal calibration of the rotation angles, despite the high precision of the estimation according to single-qubit randomized benchmarking (see Section II).

Figure 4b shows the measurements of the correlators without readout error correction. More details on the error correction procedure are provided in Section II. The results clearly demonstrate that, in the absence of readout correction, the CHSH inequality is not violated due to the significant impact of readout errors.

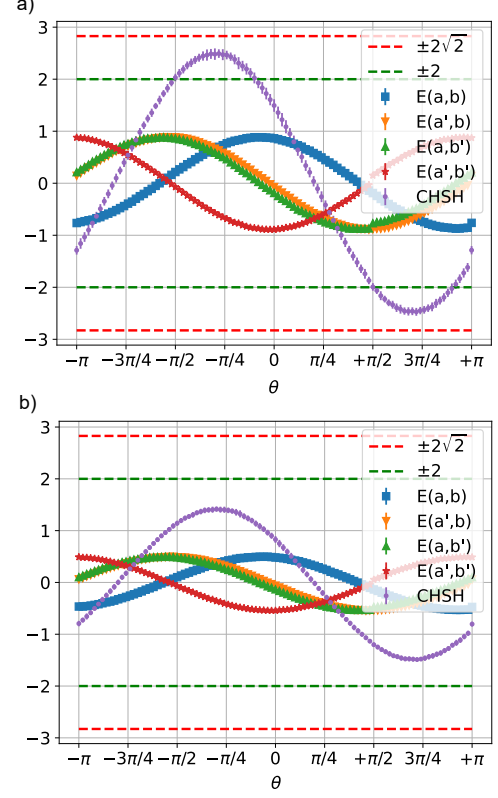


Figure 4. Correlator and CHSH values for the Bell state $\frac{1}{\sqrt{2}}(|00\rangle + |11\rangle)$ with readout error correction a) and without correction b).

V. CONCLUSIONS

This work demonstrates the application of variational quantum algorithm (VQA) to prepare entangled Bell states and Greenberger–Horne–Zeilinger (GHZ) states. By utilizing a simple variational circuit incorporating non-ideal iSwap-like gates and single-qubit X and Y rotations, we achieved high-fidelity preparation of these states. The average fidelity of the Bell’s prepared states is 0.956 ± 0.007 . For the GHZ state, the fidelity is 0.869 ± 0.003 . The key advantages of our approach lie in the simplicity of the circuit design with the minimal calibration required for the iSwap-like gates and ideal quantum evolution can be precisely reproduced using a variational circuit containing imperfect two-qubit gates.

Additionally, we experimentally measured the violation of the Clauser–Horne–Shimony–Holt (CHSH) inequality for the prepared Bell states, confirming their quantum entanglement. The observed violations exceeded the classical limit of 2, with average value 2.52 ± 0.10 .

However, scaling this direct approach to larger qubit systems becomes challenging due to the exponentially increasing tomography time for multi-qubit states. To address this, a hybrid strategy can be employed: a standard

circuit with Hadamard and CNOT gates can be used for state preparation, while the approximation of two-qubit gates can be achieved using variational circuits similar to those developed in this work.

ACKNOWLEDGMENTS

The experimental sample was fabricated at the MIPT Shared Facility Center. All authors declare no competing interests.

[1] J. Brown, M. Paternostro, and A. Ferraro, Optimal quantum control via genetic algorithms for quantum state engineering in driven-resonator mediated networks, *Quantum Science and Technology* **8**, 025004 (2023).

[2] E. Genois, N. J. Stevenson, N. Goss, I. Siddiqi, and A. Blais, Quantum optimal control of superconducting qubits based on machine-learning characterization (2024), arXiv:2410.22603 [quant-ph].

[3] J. Preskill, Quantum Computing in the NISQ era and beyond, *Quantum* **2**, 79 (2018).

[4] P. S. K. B. e. a. Sagastizabal, R., Variational preparation of finite-temperature states on a quantum computer, *npj Quantum Information* **7**, 130 (2021).

[5] D. Ristè, M. P. da Silva, C. A. Ryan, A. W. Cross, A. D. Córcoles, J. A. Smolin, J. M. Gambetta, J. M. Chow, and B. R. Johnson, Demonstration of quantum advantage in machine learning, *npj Quantum Information* **3**, 10.1038/s41534-017-0017-3 (2017).

[6] V. Havlíček, A. D. Córcoles, K. Temme, A. W. Harrow, A. Kandala, J. M. Chow, and J. M. Gambetta, Supervised learning with quantum-enhanced feature spaces, *Nature* **567**, 209–212 (2019).

[7] T. Dutta, A. Pérez-Salinas, J. P. S. Cheng, J. I. Latorre, and M. Mukherjee, Single-qubit universal classifier implemented on an ion-trap quantum device, *Physical Review A* **106**, 10.1103/physreva.106.012411 (2022).

[8] J. Herrmann, S. M. Llima, A. Remm, P. Zapletal, N. A. McMahon, C. Scarato, F. Swiadek, C. K. Andersen, C. Hellings, S. Krinner, N. Lacroix, S. Lazar, M. Kerschbaum, D. C. Zanuz, G. J. Norris, M. J. Hartmann, A. Wallraff, and C. Eichler, Realizing quantum convolutional neural networks on a superconducting quantum processor to recognize quantum phases, *Nature Communications* **13**, 10.1038/s41467-022-31679-5 (2022).

[9] A. Tolstobrov, G. Fedorov, S. Sanduleanu, S. Kadyrmetov, A. Vasenin, A. Bolgar, D. Kalacheva, V. Lubsanov, A. Dorogov, J. Zotova, P. Shlykov, A. Dmitriev, K. Tikhonov, and O. V. Astafiev, Hybrid quantum learning with data reuploading on a small-scale superconducting quantum simulator, *Phys. Rev. A* **109**, 012411 (2024).

[10] A. Tolstobrov, S. Kadyrmetov, G. Fedorov, S. Sanduleanu, V. Lubsanov, D. Kalacheva, A. Bolgar, A. Dmitriev, E. Korostylev, K. Tikhonov, and O. V. Astafiev, Integrated circuits for quantum machine learning based on superconducting artificial atoms and methods of their control, *Radiophysics and Quantum Electronics* **66** (2024).

[11] W. Ren, W. Li, S. Xu, K. Wang, W. Jiang, F. Jin, X. Zhu, J. Chen, Z. Song, P. Zhang, H. Dong, X. Zhang, J. Deng, Y. Gao, C. Zhang, Y. Wu, B. Zhang, Q. Guo, H. Li, Z. Wang, J. Biamonte, C. Song, D.-L. Deng, and H. Wang, Experimental quantum adversarial learning with programmable superconducting qubits, *Nature Computational Science* **2**, 711–717 (2022).

[12] X. Pan, Z. Lu, W. Wang, Z. Hua, Y. Xu, W. Li, W. Cai, X. Li, H. Wang, Y.-P. Song, C.-L. Zou, D.-L. Deng, and L. Sun, Deep quantum neural networks on a superconducting processor, *Nature Communications* **14**, 10.1038/s41467-023-39785-8 (2023).

[13] V. T. Hai, N. T. Viet, and L. B. Ho, Variational preparation of entangled states on quantum computers (2023), arXiv:2306.17422 [quant-ph].

[14] M. A. Nielsen and I. L. Chuang, *Quantum Computation and Quantum Information: 10th Anniversary Edition* (Cambridge University Press, 2010).

[15] M. Steffen, M. Ansmann, R. Bialczak, N. Katz, E. Lucero, R. McDermott, M. Neeley, E. Weig, A. Cleland, and J. Martinis, Direct measurement of the entanglement of two superconducting qubits via state tomography, *Science (New York, N.Y.)* **313**, 1423 (2006).

[16] M. Ansmann, H. Wang, R. Bialczak, M. Hofheinz, E. Lucero, M. Neeley, A. O’Connell, D. Sank, M. Weides, J. Wenner, A. Cleland, and J. Martinis, Violation of bell’s inequality in josephson phase qubits, *Nature* **461**, 504 (2009).

[17] L. DiCarlo, J. M. Chow, J. M. Gambetta, L. S. Bishop, B. R. Johnson, D. I. Schuster, J. Majer, A. Blais, L. Frunzio, S. M. Girvin, and R. J. Schoelkopf, Demonstration of two-qubit algorithms with a superconducting quantum processor, *Nature* **460**, 240–244 (2009).

[18] F. Arute *et al.*, Observation of separated dynamics of charge and spin in the Fermi-Hubbard model, (2020), arXiv:2010.07965 [quant-ph].

[19] B. Foxen, C. Neill, A. Dunsworth, P. Roushan, B. Chiaro, A. Megrant, J. Kelly, Z. Chen, K. Satzinger, R. Barends, F. Arute, K. Arya, R. Babbush, D. Bacon, J. C. Bardin, S. Boixo, D. Buell, B. Burkett, Y. Chen, R. Collins, E. Farhi, A. Fowler, C. Gidney, M. Giustina, R. Graff, M. Harrigan, T. Huang, S. V. Isakov, E. Jeffrey, Z. Jiang, D. Kafri, K. Kechedzhi, P. Klimov, A. Korotkov, F. Kostritsa, D. Landhuis, E. Lucero, J. McClean, M. McEwen, X. Mi, M. Mohseni, J. Y. Mutus, O. Naaman, M. Neeley, M. Niu, A. Petukhov, C. Quintana, N. Rubin, D. Sank, V. Smelyanskiy, A. Vainsencher, T. C. White, Z. Yao, P. Yeh, A. Zalcman, H. Neven, and J. M. Martinis (Google AI Quantum), Demonstrating a continuous set of two-qubit gates for near-term quantum algorithms, *Phys. Rev. Lett.* **125**, 120504 (2020).

[20] Y.-x. Liu, L. F. Wei, and F. Nori, Tomographic measurements on superconducting qubit states, *Phys. Rev. B* **72**, 014547 (2005).

[21] J. S. Bell, On the einstein podolsky rosen paradox, *Physics Physique Fizika* **1**, 195 (1964).

[22] A. Einstein, B. Podolsky, and N. Rosen, Can quantum-mechanical description of physical reality be considered complete?, *Phys. Rev.* **47**, 777 (1935).

[23] J. F. Clauser, M. A. Horne, A. Shimony, and R. A. Holt, Proposed experiment to test local hidden-variable theo-

ries, Phys. Rev. Lett. **23**, 880 (1969).

[24] J. Koch, T. M. Yu, J. Gambetta, A. A. Houck, D. I. Schuster, J. Majer, A. Blais, M. H. Devoret, S. M. Girvin, and R. J. Schoelkopf, Charge-insensitive qubit design derived from the cooper pair box, Phys. Rev. A **76**, 042319 (2007).

[25] F. Motzoi, J. M. Gambetta, P. Rebentrost, and F. K. Wilhelm, Simple pulses for elimination of leakage in weakly nonlinear qubits, Phys. Rev. Lett. **103**, 110501 (2009).

[26] J. M. Gambetta, F. Motzoi, S. T. Merkel, and F. K. Wilhelm, Analytic control methods for high-fidelity unitary operations in a weakly nonlinear oscillator, Phys. Rev. A **83**, 012308 (2011).

[27] E. Knill, D. Leibfried, R. Reichle, J. Britton, R. B. Blakestad, J. D. Jost, C. Langer, R. Ozeri, S. Seidelin, and D. J. Wineland, Randomized benchmarking of quantum gates, Physical Review A **77**, 10.1103/physreva.77.012307 (2008).

[28] Y. Chen, D. Sank, P. O’Malley, T. White, R. Barends, B. Chiaro, J. Kelly, E. Lucero, M. Mariantoni, A. Megrant, C. Neill, A. Vainsencher, J. Wenner, Y. Yin, A. N. Cleland, and J. M. Martinis, Multiplexed dispersive readout of superconducting phase qubits, Applied Physics Letters **101**, 10.1063/1.4764940 (2012).

[29] T. Walter, P. Kurpiers, S. Gasparinetti, P. Magnard, A. Potočnik, Y. Salathé, M. Pechal, M. Mondal, M. Oppliger, C. Eichler, and A. Wallraff, Rapid high-fidelity single-shot dispersive readout of superconducting qubits, Phys. Rev. Appl. **7**, 054020 (2017).

[30] A. Dorogov, G. Fedorov, D. Kalacheva, A. Dmitriev, A. Bolgar, N. Abramov, and O. Astafiev, Application of a broadband josephson parametric amplifier, St Petersburg Polytechnical University Journal Physics and Mathematics **15** (2022).

[31] F. B. Maciejewski, Z. Zimborás, and M. Oszmaniec, Mitigation of readout noise in near-term quantum devices by classical post-processing based on detector tomography, Quantum **4**, 257 (2020).

[32] D. S. Lvov, S. A. Lemziakov, E. Ankerhold, J. T. Peltonen, and J. P. Pekola, Thermometry based on a superconducting qubit (2025), arXiv:2409.02784 [quant-ph].

[33] K. Geerlings, Z. Leghtas, I. M. Pop, S. Shankar, L. Frunzio, R. J. Schoelkopf, M. Mirrahimi, and M. H. Devoret, Demonstrating a driven reset protocol for a superconducting qubit, Physical Review Letters **110**, 10.1103/physrevlett.110.120501 (2013).

[34] P. Magnard, P. Kurpiers, B. Royer, T. Walter, J.-C. Besse, S. Gasparinetti, M. Pechal, J. Heinsoo, S. Storz, A. Blais, and A. Wallraff, Fast and unconditional all-microwave reset of a superconducting qubit, Physical Review Letters **121**, 10.1103/physrevlett.121.060502 (2018).

[35] Y. Nesterov, A method for solving the convex programming problem with convergence rate $\mathcal{O}(1/k^2)$, Proceedings of the USSR Academy of Sciences **269**, 543 (1983).

[36] K. Mitarai, M. Negoro, M. Kitagawa, and K. Fujii, Quantum circuit learning, Phys. Rev. A **98**, 032309 (2018).

[37] M. Schuld, V. Bergholm, C. Gogolin, J. A. Izaac, and N. Killoran, Evaluating analytic gradients on quantum hardware, Physical Review A (2018).

[38] V. Bergholm, J. Izaac, M. Schuld, C. Gogolin, S. Ahmed, V. Ajith, M. S. Alam, G. Alonso-Linaje, B. Akash-Narayanan, A. Asadi, J. M. Arrazola, U. Azad, S. Banning, C. Blank, T. R. Bromley, B. A. Cordier, J. Cerón, A. Delgado, O. D. Matteo, A. Dusko, T. Garg, D. Gual, A. Hayes, R. Hill, A. Ijaz, T. Isacsson, D. Ittah, S. Jhangiri, P. Jain, E. Jiang, A. Khandelwal, K. Kottmann, R. A. Lang, C. Lee, T. Loke, A. Lowe, K. McKiernan, J. J. Meyer, J. A. Montañez-Barrera, R. Moyard, Z. Niu, L. J. O’Riordan, S. Oud, A. Panigrahi, C.-Y. Park, D. Polatajko, N. Quesada, C. Roberts, N. Sá, I. Schoch, B. Shi, S. Shu, S. Sim, A. Singh, I. Strandberg, J. Soni, A. Száva, S. Thabet, R. A. Vargas-Hernández, T. Vincent, N. Vitucci, M. Weber, D. Wierichs, R. Wiersema, M. Willmann, V. Wong, S. Zhang, and N. Killoran, PennyLane: Automatic differentiation of hybrid quantum-classical computations (2022), arXiv:1811.04968 [quant-ph].

[39] B. S. Cirel’son, Quantum generalizations of bell’s inequality, Letters in Mathematical Physics **4**, 93 (1980).

**Supplementary materials for Variational preparation of entangled states in
a system of transmon qubits**

I. EXPERIMENTAL SAMPLE

This section provides an overview of the experimental sample used in the study. The illustrations include:

- A 16-transmon quantum processor, with a focus on the three qubits involved in the experiment (highlighted in Figure 1a).
- A micrograph of the chip bonded into a holder (Figure 1b).

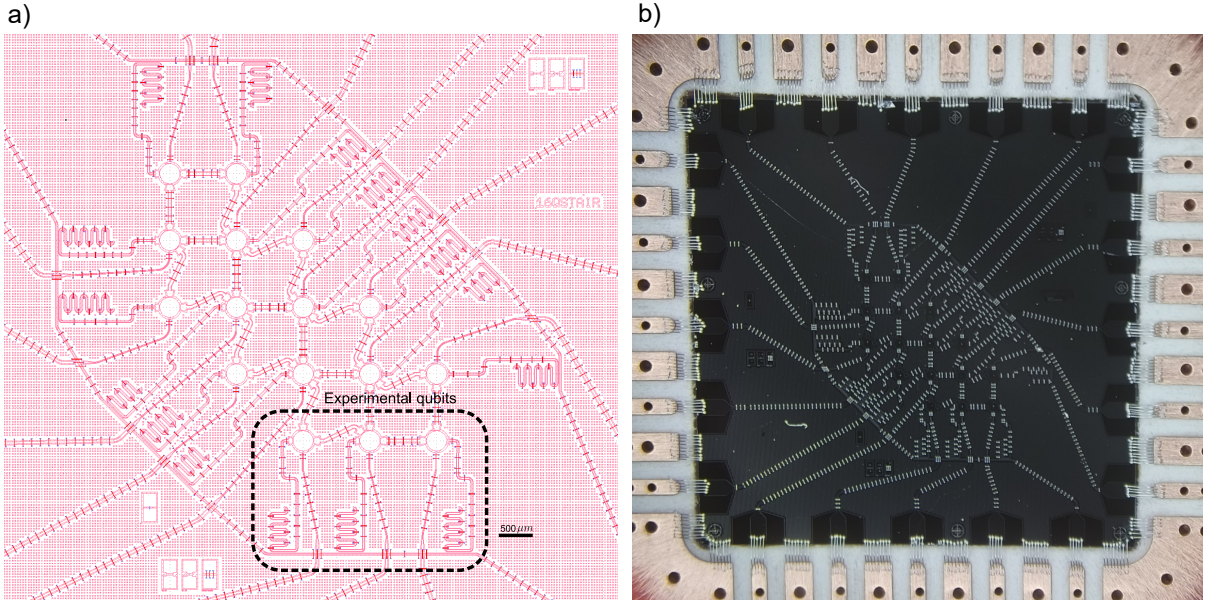


FIG. 1. a) Schematic of the 16-transmon quantum processor. The three qubits used in the experiment are highlighted within the dotted-line boundary. b) Micrograph of the chip bonded into a holder.

II. CALIBRATION OF ISWAP-LIKE TWO-QUBIT GATE

The calibration of the two-qubit iSwap-like operation was performed as follows. We excite one of the qubits from level $|0\rangle$ to $|1\rangle$ and drive two qubits into resonance to observe oscillations between $|01\rangle$ and $|10\rangle$ qubit states, which can be seen in Figure 2. Thus using two parameters, the operation time and the amplitude of the flux pulse, we find the point of maximum population transfer between states $|01\rangle$, $|10\rangle$, as depicted in Figure 2.

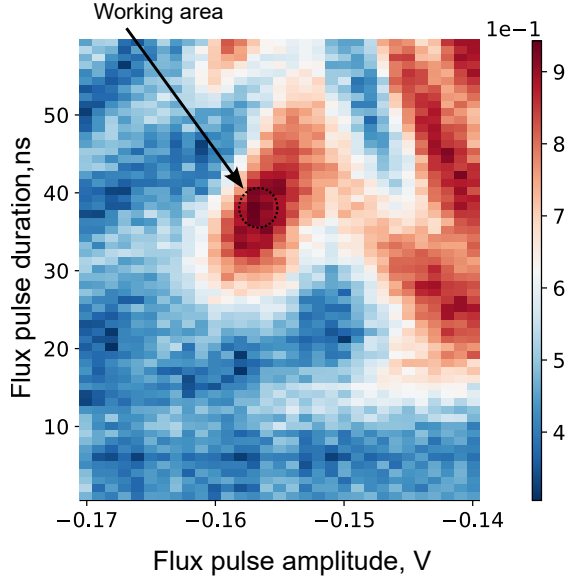


FIG. 2. iSwap-like gate calibration. The arrow shows the area of maximum transfer of populations between the $|01\rangle$, $|10\rangle$ transmon levels.

III. TOMOGRAPHY OF ISWAP-LIKE TWO-QUBIT GATE

Quantum process tomography [1] was used to understand the appearance of simple calibrated two-qubit iSwap-like gates. Then, a two-qubit gait approximation [2] was performed to best fit the resulting process matrices.

We approximate the matrix of a two-qubit quantum operation by the 1 model. Obtained parameter values for iSwap-like operation: $\theta = 1.52$, $\phi = 1.21$, $\Delta_+ = -1.69$, $\Delta_- = 0.41$, $\Delta_{-,off} = 0.15$. The fidelity we define as $\mathcal{F} = \sqrt{\text{Tr}(M_{exp} \cdot M_{targ})}$ (M_{exp} is the measured matrix of the quantum process, M_{targ} is the target matrix of the quantum process) of the two-qubit gate (see Figure 3). Fidelity of the approximation of the process matrix: $\mathcal{F}_{final} = 0.89$. Fidelity of the identity operation: $\mathcal{F}_{id} = 0.93$. To estimate the effect of reading errors on tomography, it will be assumed that the resulting fidelity is equal to $\mathcal{F}_{final} = \mathcal{F}_{id} \cdot \mathcal{F}_{iSwap-like}$. Thus the approximation fidelity of the iSwap-like operation is equal to $\mathcal{F}_{iSwap-like} = 0.96$.

It can be seen that iSwap parameter θ is close to $\pi/2$, which is in agreement with our simple calibration. But the iSwap-like operation also has a phase from the cPhase operation and single-qubit phases.

iSwap-like $(\theta, \phi, \Delta_+, \Delta_-, \Delta_{-,off}) =$

$$\begin{pmatrix} 1 & 0 & 0 & 0 \\ 0 & e^{i(\Delta_+ + \Delta_-)} \cos \theta & -ie^{i(\Delta_+ - \Delta_{-,off})} \sin \theta & 0 \\ 0 & -ie^{i(\Delta_+ + \Delta_{-,off})} \sin \theta & e^{i(\Delta_+ - \Delta_-)} \cos \theta & 0 \\ 0 & 0 & 0 & e^{i(2\Delta_+ + \phi)} \end{pmatrix} \quad (1)$$

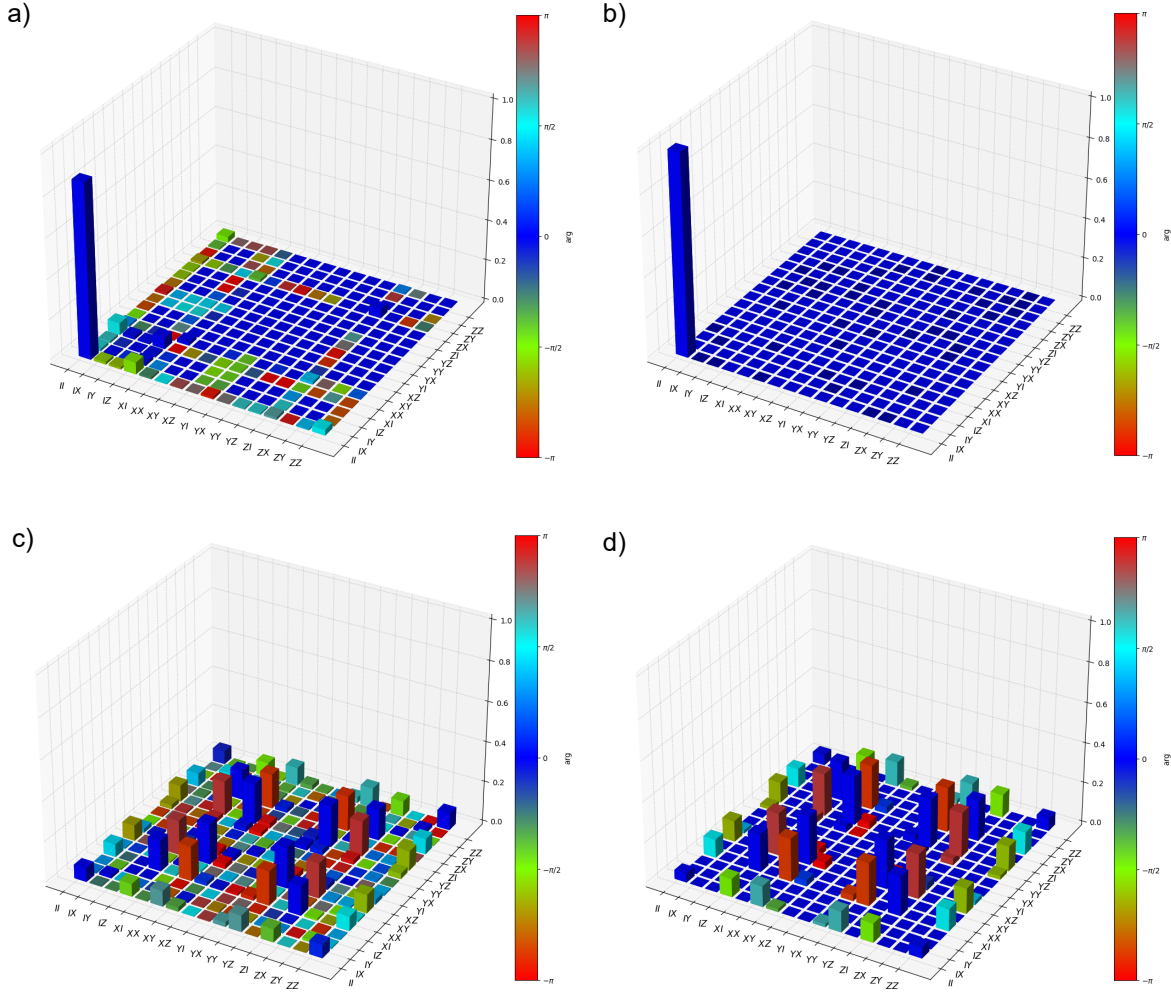


FIG. 3. a)-b) Tomography of the identity operation. Fidelity of tomography: 0.93. c)-d) Tomography of the two-qubit iSwap-like operation and approximation using 1 matrix. Obtained parameter values: $\theta = 1.52$, $\phi = 1.21$, $\Delta_+ = -1.69$, $\Delta_- = 0.41$, $\Delta_{-,off} = 0.15$. Fidelity of the approximation of the process matrix: 0.89.

IV. RESULTS OF PREPARATION OF BELL STATES AND GHZ STATE

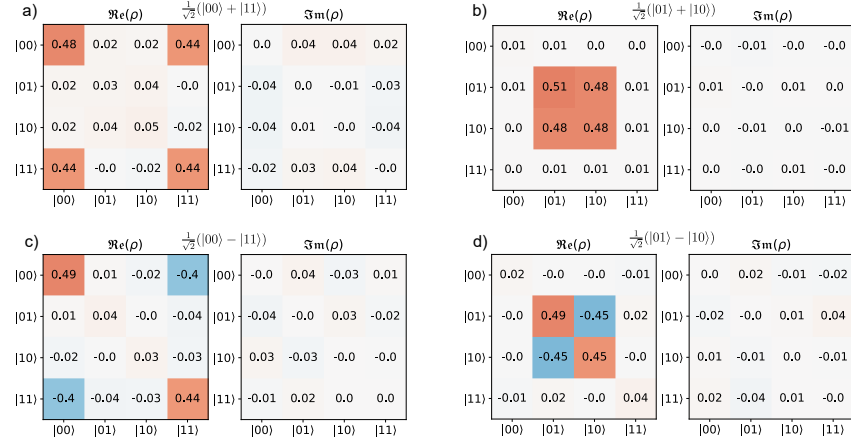


FIG. 4. Measured density matrices, their real and imaginary parts, for 4 Bell states.

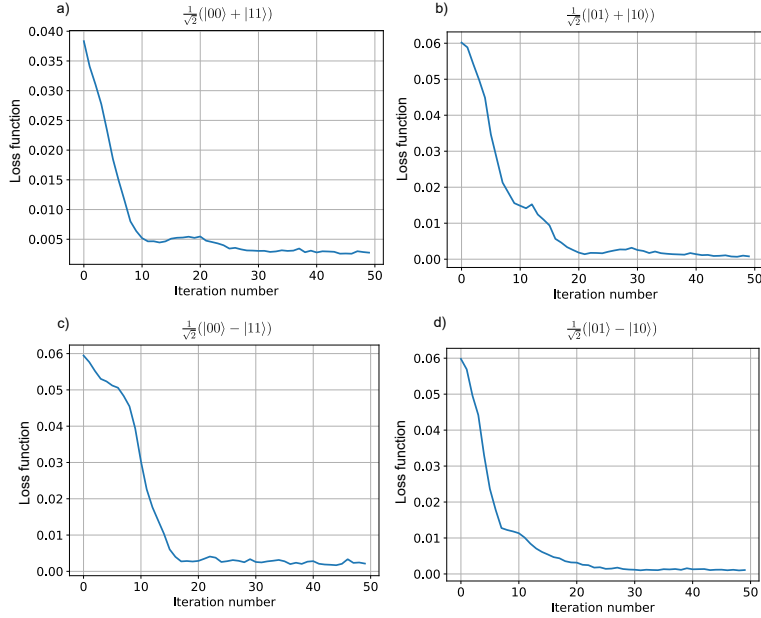


FIG. 5. Dependencies of the loss function on the number of iterations of the optimization algorithm for 4 Bell states.

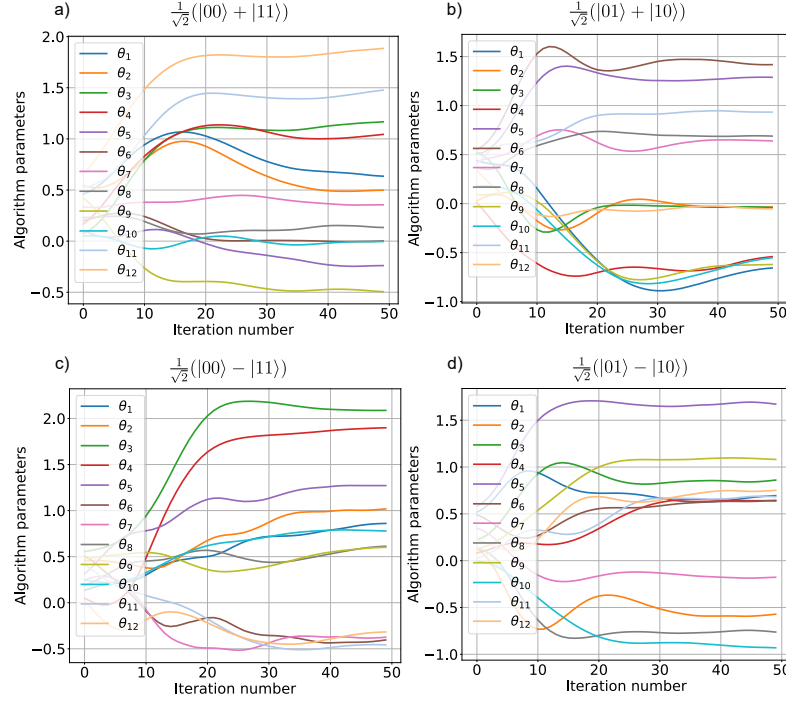


FIG. 6. Evolution of the optimized parameters of the algorithm from the iteration number for 4 Bell states.

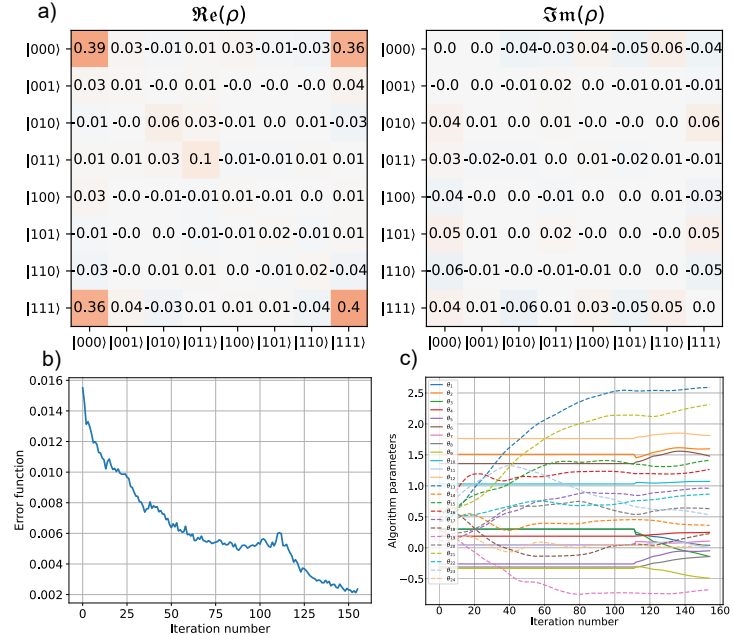


FIG. 7. a) Measured density matrix for three-qubit GHZ state. b) Dependencies of the loss function on the number of iterations of the optimization algorithm for GHZ state. c) Evolution of the optimized parameters of the algorithm from the iteration number for GHZ state.

V. RESULTS OF MEASURING OF CHSH INEQUALITY VIOLATION

The Figure 8 shows the measured violations of the CHSH inequality for all 4 prepared Bell states.

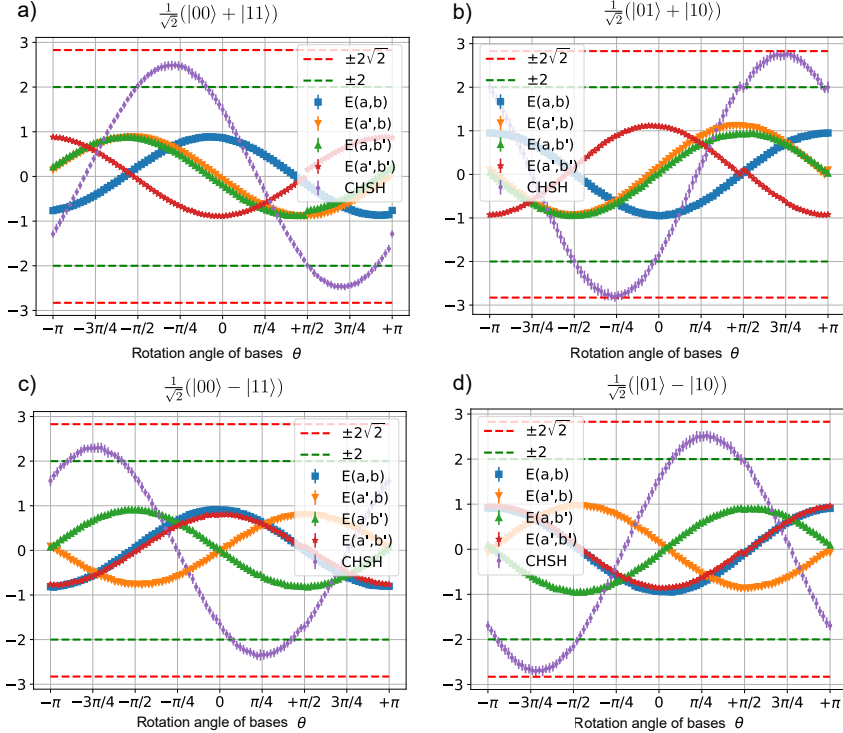


FIG. 8. Measured correlators and CHSH expression for 4 Bell states.

- [1] Y.-x. Liu, L. F. Wei, and F. Nori, Tomographic measurements on superconducting qubit states, *Phys. Rev. B* **72**, 014547 (2005).
- [2] B. Foxen, C. Neill, A. Dunsworth, P. Roushan, B. Chiaro, A. Megrant, J. Kelly, Z. Chen, K. Satzinger, R. Barends, F. Arute, K. Arya, R. Babbush, D. Bacon, J. C. Bardin, S. Boixo, D. Buell, B. Burkett, Y. Chen, R. Collins, E. Farhi, A. Fowler, C. Gidney, M. Giustina, R. Graff, M. Harrigan, T. Huang, S. V. Isakov, E. Jeffrey, Z. Jiang, D. Kafri, K. Kechedzhi, P. Klimov, A. Korotkov, F. Kostritsa, D. Landhuis, E. Lucero, J. McClean, M. McEwen, X. Mi, M. Mohseni, J. Y. Mutus, O. Naaman, M. Neeley, M. Niu, A. Petukhov, C. Quintana, N. Rubin, D. Sank, V. Smelyanskiy, A. Vainsencher, T. C. White, Z. Yao, P. Yeh, A. Zalcman, H. Neven, and J. M. Martinis (Google AI Quantum), Demonstrating a continuous set of two-qubit gates for near-term quantum algorithms, *Phys. Rev. Lett.* **125**, 120504 (2020).